machines

Article

Vibration Attenuation in a Beam Structure with a Periodic Free-Layer Damping Treatment

Zhiwei Guo [1,2], Meiping Sheng [1,2,*] and Hao Zeng [1,2]

1 School of Marine Science and Technology, Northwestern Polytechnical University, Xi'an 710072, China; gzw@nwpu.edu.cn (Z.G.); zengh@mail.nwpu.edu.cn (H.Z.)
2 Ningbo Institute of Northwestern Polytechnical University, Ningbo 315103, China
* Correspondence: acoustics@nwpu.edu.cn

Abstract: In order to improve the vibration reduction performance of damping treatments, a new damping structure consisting of a uniform base layer and two periodically alternating free layers was examined in this study. Closed-form solutions for both the band structure and the forced response of the periodic bi-layer beam were theoretically derived and verified via numerical solutions using the finite-element method. The results showed that the structure with periodic free-layer damping (PFLD) treatment reduced broadband vibrations, and the levels of reduction were dominated by Bragg scattering in the band gaps and damping in the passbands. The vibration experiment verified the derived theory's accuracy and showed that the PFLD treatment could increase vibration reduction levels in low-frequency band gaps compared with traditional free-layer damping treatments. The effects of the parameters—cell lengths, sub-cell-length ratios, and thickness ratios—were also discussed, providing further understanding of the vibration reduction performance of the bi-layer beam with the PFLD treatment, and this can be used to help designers optimize the periodic bi-layer beam to achieve better performance.

Keywords: periodic bi-layer beam; band gap; vibration control; propagation constant; damping treatment

check for updates

Citation: Guo, Z.; Sheng, M.; Zeng, H. Vibration Attenuation in a Beam Structure with a Periodic Free-Layer Damping Treatment. *Machines* **2023**, *11*, 949. https://doi.org/10.3390/machines11100949

Academic Editor: Vincenzo Niola

Received: 30 August 2023
Revised: 28 September 2023
Accepted: 4 October 2023
Published: 11 October 2023

Copyright: © 2023 by the authors. Licensee MDPI, Basel, Switzerland. This article is an open access article distributed under the terms and conditions of the Creative Commons Attribution (CC BY) license (https://creativecommons.org/licenses/by/4.0/).

1. Introduction

As thin-walled flexible structures easily vibrate and thereby radiate excessive noise, various vibration and noise reduction methods, in which applying damping treatments are of great importance, have been proposed and used in engineering. Free-layer damping (FLD) treatments [1–3] and constraint-layer damping (CLD) treatments [4–6] have been considered two of the main implementation methods, and these damping treatments have been widely used in engineering, including—but not limited to—aircraft skins, submarine hulls, and automobile panels [7–9].

Due to its low cost, easy design, and high reliability, the FLD treatment has won the recognition of both researchers and engineers since it was introduced by Oberst [10]. The FLD treatment is the most straightforward configuration for introducing damping into structures. In an FLD treatment, a viscoelastic material (VEM) is freely attached to the surface of a flexible structure. Due to the alternating extension and compression of the damping layer, the vibration energy can be dissipated in an FLD treatment, thus reducing excessive vibration and noise.

Although the FLD treatment is convenient to implement, its damping dissipation ability needs to be improved to further reduce vibration energy. Thus, various damping structures have been proposed, studied, and implemented in engineering applications, such as constraint-layer damping structures, multiple-damping-layer structures, and irregular-damping structures [11]. By using these improved passive damping structures, vibrations can be further reduced. The vibration reductions arising from these damping treatments are caused by the energy dissipation introduced by the VEM in the damping layer. However, the vibration reduction performances of current damping structures vary with frequency [12]. The wave attenuation in the low-frequency domain is inferior to that in the high-frequency domain, owing to the larger wavelengths of low-frequency waves, where the strain energy dissipated per unit of length in the low-frequency domain is significantly reduced compared with that in the high-frequency domain.

In order to improve the low-frequency vibration performance, smart CLD (SCLD) treatments or active CLD (ACLD) treatments have been researched in recent years [13,14], where the elastic constraint layer is replaced by piezoelectric or smart materials. Through passive control from the viscoelastic material and active control from the piezoelectric material, the attenuation performance can be improved in a broader frequency range. However, due to their complicated control strategies and high costs, the SCLD and ACLD treatments cannot be widely used in various engineering applications. Hence, new control methods for damping structures require further investigation.

In recent decades, phononic crystals and acoustic metamaterials have been extensively studied due to their remarkable abilities in controlling vibrations and noise [15–17], and they have provided new ways to improve the attenuation performance of a damping structure. Phononic crystals and acoustic metamaterials generally consist of periodic cells, and they can generate band gaps because of their periodicity. The waves can be significantly reduced in the band gaps due to the Bragg scattering effect [18] or the locally resonant effect [19].

Most previous works on periodic structures, including phononic crystals and acoustic metamaterials, have focused on single-layer periodic structure types, where each cell is joined end to end to another. These studies have included periodic single-layer beams [20], plates [21], and shell [22] structures, and they have provided essential methods, mechanisms, or conclusions. Only a few studies have focused on multi-layer periodic structures [23–25]. However, most of the above studies were based on numerical calculation methods without analytical solutions or experimental verification. Unknown mechanisms, phenomena, or possible applications in the multi-layer periodic structures remain, and their vibration attenuation characteristics need to be further analyzed, although a number of studies on single-layer periodic structures have been conducted.

In order to promote the study of the vibrations of multi-layer periodic structures, in a past study, the authors extended the single-layer structure to a bi-layer structure [26], where the band-gap performance and vibration reduction characteristics of a bi-layer periodic beam consisting of a four-component cell were studied. The considered structure (Figure 1) performed well with a broad band-gap width and provided more band-gap tuning possibilities. However, in a practical application, this structure generally could not bear too great a load as each sub-cell was typically bonded to others by glue. In addition, the upper and bottom layers were considered to have identical rotations in the theoretical model for the purpose of concision. Thus, the model was only appropriate for a structure whose upper-layer material parameters did not significantly differ from those of its bottom layer. Moreover, the previous model did not consider damping, and its vibration reduction was generally induced by Bragg scattering.

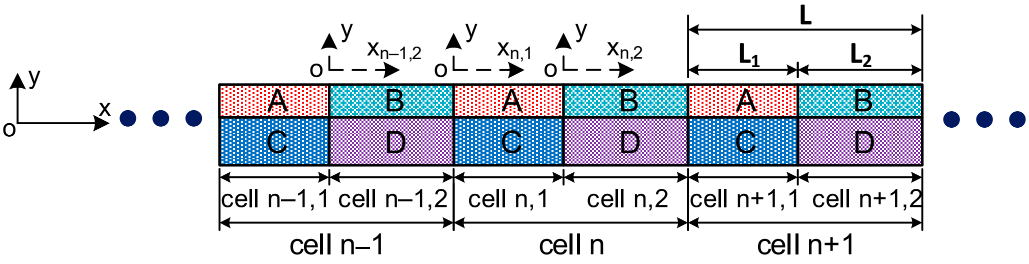

Figure 1. A sketch map of the four-component periodic bi-layer beam from a previous study [26].

In previous studies, damping treatment research and band-gap structure research have been separated as two independent research domains, and few relevant studies combining the two exist. Integrating the attenuation advantages of both band-gap structures and damping structures will have important implications for vibration reduction. In order to broaden the practical vibration reduction applications of periodic bi-layer structures in engineering, the authors' previous work [26] was extended in this study.

In this paper, a new concept for damping treatments, namely a periodic free-layer damping (PFLD) treatment, is proposed. In PFLD, a hard VEM and a soft VEM are alternated along the axial direction and are bonded upon a base layer. The considered structure has been improved from the previous four-component type to a three-component type, where components C and D, as shown in Figure 1, are replaced with a homogeneous material. In the present theoretical model, the upper layer and bottom layer rotations were considered to be two independent variables, and the order of the bi-layer beam's partial differential equation was increased from six to eight, allowing for the material parameters of both layers to have considerable differences. In addition, the damping parameter was also considered in the new model by using a complex modulus. By appropriately tuning the material or geometric parameters, PFLD was able to provide better vibration attenuation performances over a broader frequency range through both the Bragg scattering and damping effects. Owing to its superior attenuation performance, this PFLD structure may have great potential in reducing vibrations in aircraft skins, submarine hulls, and automobile panels in the future.

2. Theory and Formulations

2.1. Description of the Bi-Layer Beam

A model of the bi-layer beam with an elastic base layer and a viscoelastic free layer is shown in Figure 2. The following assumptions were considered in establishing the theoretical model: (a) the bottom layer comprised a linear elastic material, and the upper layer was a linear VEM with complex Young's and shear moduli; (b) the upper and lower layers were modeled as Timoshenko beams, including the effects of shear deformation, rotatory inertia, and longitudinal deformation; (c) slipping did not occur between the upper and bottom layers; and (d) the transverse displacements in both layers were identical at the same position along the axial direction.

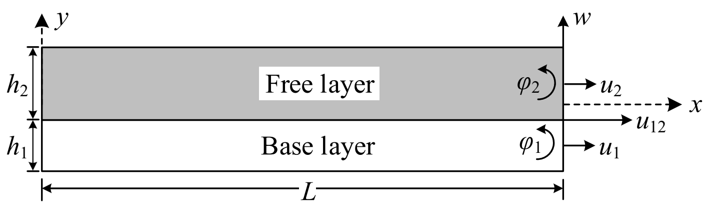

Figure 2. Coordinates of and notations for the bi-layer beam.

The material parameters of the bi-layer beam are specified by the Young's modulus E_i, shear modulus G_i, density ρ_i, Poisson's ratio v_i, and shear coefficient $k_i = 5/6$ [27], where $i = 1, 2$. The upper layer is considered to be a linear viscoelastic model with complex Young's modulus $E_2 = E_{2s}(1 + j\eta)$ and shear modulus $G_2 = G_{2s}(1 + j\eta)$, where E_{2s} and G_{2s} are the storage moduli, and η is the structural loss factor. The bi-layer beam's length, width, and thickness are specified as L, b, and h_i, respectively. The transverse displacement, longitudinal displacement, and local rotation of each layer are specified as w, u_i, and φ_i, respectively.

2.2. The Dynamic Stiffness Theory

As the longitudinal displacement at the interface between the upper and bottom layers can be expressed as $u_{12} = u_1 + h_1\varphi_1/2 = u_2 - h_2\varphi_2/2$, the longitudinal displacement u_2 can be given as $u_2 = u_1 + h_1\varphi_1/2 + h_2\varphi_2/2$. The total strain energy E_{pot} and total kinematic energy E_{kin} can be obtained by referring to references [28,29], and they can be expressed as follows:

$$\begin{cases} E_{\text{pot}} = \frac{1}{2}\sum\limits_{i=1}^{2} \int_0^L \left[E_i A_i u_i'^2 + E_i I_i \varphi_i'^2 + k_i G_i A_i (w' - \varphi_i)^2\right] \mathrm{d}x \\ E_{\text{kin}} = \frac{1}{2}\sum\limits_{i=1}^{2} \int_0^L \left[\rho_i A_i \left(\dot{w}^2 + \dot{u}_i^2\right) + \rho_i I_i \dot{\varphi}_i^2\right] \mathrm{d}x \end{cases}, \quad (1)$$

where $A_i = bh_i$ and $I_i = bh_i^3/12$ are the cross-sectional area and area moment of inertia, respectively. The dots and primes in Equation (1) denote partial differentiation with respect to the time variable t and space variable x, respectively. The work carried out by the external force can be expressed as follows:

$$W_e = (N_1 u_1 + M_1 \varphi_1 + M_2 \varphi_2 + Qw)\Big|_0^L, \quad (2)$$

where N_1 is the base layer's axial force, M_i is the i^{th} layer's bending moment, and Q is the total shearing force. By using Hamilton's principle ($\delta \int_{t_0}^{t_1} (E_{\text{kin}} - E_{\text{pot}} - W_{\text{e}}) \mathrm{d}t = 0$) and the harmonic oscillation assumptions $u_1 = U_1 \mathrm{e}^{\mathrm{j}\omega t}$, $\varphi_1 = \Phi_1 \mathrm{e}^{\mathrm{j}\omega t}$, $\varphi_2 = \Phi_2 \mathrm{e}^{\mathrm{j}\omega t}$, and $w = W\mathrm{e}^{\mathrm{j}\omega t}$, the equations of motion of the bi-layer beam can be obtained as follows:

$$\begin{cases} a_{11}\mathrm{D}\Phi_1 + a_{12}\mathrm{D}\Phi_2 + \left(a_{13} + a_{14}\mathrm{D}^2\right)W = 0 \\ \left(a_{21} + a_{22}\mathrm{D}^2\right)U_1 + \left(a_{23} + a_{24}\mathrm{D}^2\right)\Phi_1 + \left(a_{25} + a_{26}\mathrm{D}^2\right)\Phi_2 = 0 \\ \left(a_{31} + a_{32}\mathrm{D}^2\right)U_1 + \left(a_{33} + a_{34}\mathrm{D}^2\right)\Phi_1 + \left(a_{35} + a_{36}\mathrm{D}^2\right)\Phi_2 + a_{37}\mathrm{D}W = 0 \\ \left(a_{41} + a_{42}\mathrm{D}^2\right)U_1 + \left(a_{43} + a_{44}\mathrm{D}^2\right)\Phi_1 + \left(a_{45} + a_{46}\mathrm{D}^2\right)\Phi_2 + a_{47}\mathrm{D}W = 0 \end{cases}, \quad (3)$$

and the corresponding generalized forces can be given as follows:

$$\begin{cases} N_1 = a_{22}\mathrm{D}U_1 + a_{24}\mathrm{D}\Phi_1 + a_{26}\mathrm{D}\Phi_2 \\ M_1 = a_{24}\mathrm{D}U_1 + a_{34}\mathrm{D}\Phi_1 + a_{36}\mathrm{D}\Phi_2 \\ M_2 = a_{26}\mathrm{D}U_1 + a_{36}\mathrm{D}\Phi_1 + a_{46}\mathrm{D}\Phi_2 \\ Q = -a_{11}\Phi_1 - a_{12}\Phi_2 + (a_{11} + a_{12})\mathrm{D}W \end{cases}, \quad (4)$$

where D is the differential operator, defined as $\mathrm{D} = \mathrm{d}/\mathrm{d}x$, and the coefficients a_{ij} are defined in Equations (A1)–(A24) in Appendix A.

The four second-order differential equations can be simplified to a single eighth-order differential equation as follows:

$$\left(\mathrm{D}^8 + c_1\mathrm{D}^6 + c_2\mathrm{D}^4 + c_3\mathrm{D}^2 + c_4\right)X = 0, \quad (5)$$

where X can be any of U_1, Φ_1, Φ_2, and W. The coefficients c_1 to c_4 can be expressed by the coefficients a_{ij} in Equations (A1)–(A24). The solution form of Equation (5) can be assumed as $X = X_0\mathrm{e}^{rx}$, and substituting it into Equation (5) yields the following:

$$r^8 + c_1 r^6 + c_2 r^4 + c_3 r^2 + c_4 = 0. \quad (6)$$

By solving the above polynomial equation, eight roots (r_1 to r_8) can be obtained. The generalized displacements $\mathbf{d}(x) = [U_1(x), \Phi_1(x), \Phi_2(x), W(x)]^{\mathrm{T}}$ and the generalized forces $\mathbf{t}(x) = [N_1(x), M_1(x), M_2(x), W(x)]^{\mathrm{T}}$ can then be expressed as follows:

$$\begin{cases} \mathbf{d}(x) = \mathbf{D}(x)\boldsymbol{\varphi} \\ \mathbf{t}(x) = \mathbf{T}(x)\boldsymbol{\varphi} \end{cases}, \quad (7)$$

where $\mathbf{D}(x)$ and $\mathbf{T}(x)$ are two matrices with four rows and eight columns, given in Appendix A. The term $\boldsymbol{\varphi}$ is given as $\boldsymbol{\varphi} = \begin{bmatrix} \psi_1 & \psi_2 & \cdots & \psi_8 \end{bmatrix}^{\mathrm{T}}$.

For convenience, the generalized displacements and forces at the left end of the bi-layer beam are denoted as $\mathbf{d}_{\mathrm{L}} = \mathbf{D}_{\mathrm{L}}\boldsymbol{\varphi}$ and $\mathbf{t}_{\mathrm{L}} = \mathbf{T}_{\mathrm{L}}\boldsymbol{\varphi}$, respectively, where $\mathbf{D}_{\mathrm{L}} = \mathbf{D}(0)$ and $\mathbf{T}_{\mathrm{L}} = \mathbf{T}(0)$. The corresponding generalized displacements and forces at the right beam end are denoted as $\mathbf{d}_{\mathrm{R}} = \mathbf{D}_{\mathrm{R}}\boldsymbol{\varphi}$ and $\mathbf{t}_{\mathrm{R}} = \mathbf{T}_{\mathrm{R}}\boldsymbol{\varphi}$, respectively, where $\mathbf{D}_{\mathrm{R}} = \mathbf{D}(L)$ and $\mathbf{T}_{\mathrm{R}} = \mathbf{T}(L)$.

2.3. Band Structure

A unit cell of the bi-layer beam is shown in Figure 3, and it consists of sub-cell A and sub-cell B with lengths of L_{A} and L_{B}, respectively.

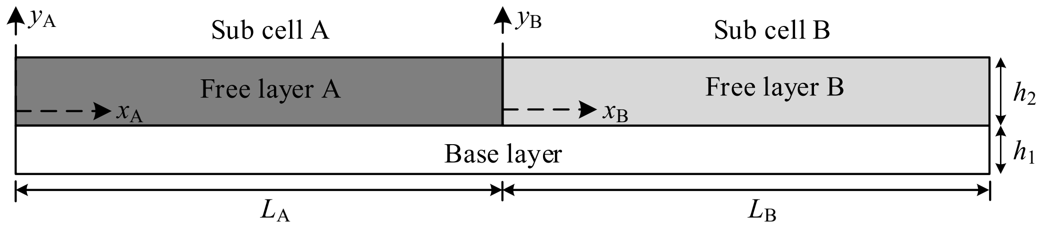

Figure 3. A unit cell of the bi-layer beam with the PFLD structure.

According to Equation (7), the generalized displacements and forces at both ends of sub-cell A and sub-cell B can be expressed as follows:

$$\begin{cases} \mathbf{d}_{\mathrm{AL}} = \mathbf{D}_{\mathrm{AL}}\boldsymbol{\varphi}_{\mathrm{A}};\ \ \mathbf{d}_{\mathrm{AR}} = \mathbf{D}_{\mathrm{AR}}\boldsymbol{\varphi}_{\mathrm{A}};\ \ \mathbf{t}_{\mathrm{AL}} = \mathbf{T}_{\mathrm{AL}}\boldsymbol{\varphi}_{\mathrm{A}};\ \ \mathbf{t}_{\mathrm{AR}} = \mathbf{T}_{\mathrm{AR}}\boldsymbol{\varphi}_{\mathrm{A}} \\ \mathbf{d}_{\mathrm{BL}} = \mathbf{D}_{\mathrm{BL}}\boldsymbol{\varphi}_{\mathrm{B}};\ \ \mathbf{d}_{\mathrm{BR}} = \mathbf{D}_{\mathrm{BR}}\boldsymbol{\varphi}_{\mathrm{B}};\ \ \mathbf{t}_{\mathrm{BL}} = \mathbf{T}_{\mathrm{BL}}\boldsymbol{\varphi}_{\mathrm{B}};\ \ \mathbf{t}_{\mathrm{BR}} = \mathbf{T}_{\mathrm{BR}}\boldsymbol{\varphi}_{\mathrm{B}} \end{cases}, \tag{8}$$

where $\boldsymbol{\varphi}_{\mathrm{A}}$ and $\boldsymbol{\varphi}_{\mathrm{B}}$ are the coefficient vectors of sub-cells A and B, respectively. At the interface between sub-cell A and sub-cell B ($x_{\mathrm{A}} = 1$ or $x_{\mathrm{B}} = 0$), the generalized displacements and forces satisfy the continuous condition and equilibrium condition, indicating the following:

$$\begin{cases} \mathbf{d}_{\mathrm{AR}} = \mathbf{d}_{\mathrm{BL}} \\ \mathbf{t}_{\mathrm{AR}} = -\mathbf{t}_{\mathrm{BL}} \end{cases}. \tag{9}$$

By using the Bloch–Floquet periodic conditions [30],

$$\begin{cases} \mathbf{d}_{\mathrm{AL}} = \mathrm{e}^{-\mu}\mathbf{d}_{\mathrm{BR}} \\ \mathbf{t}_{\mathrm{AL}} = -\mathrm{e}^{-\mu}\mathbf{t}_{\mathrm{BR}} \end{cases}, \tag{10}$$

the characteristic equation for calculating the band structure can be obtained as follows:

$$(\mathbf{T} - \mathrm{e}^{\mu}\mathbf{I})\boldsymbol{\varphi}_{\mathrm{A}} = \mathbf{0}, \tag{11}$$

where $\mu = \delta + \mathrm{j}\gamma$ is the propagation constant in which δ is the decay constant and γ is the phase constant [31]. In Equation (11), $\mathbf{I}$ is an eight-by-eight identity matrix and $\mathbf{T} = \mathbf{K}_3^{-1}\mathbf{K}_4\mathbf{K}_2^{-1}\mathbf{K}_1$, where $\mathbf{K}_1 = \begin{bmatrix} \mathbf{D}_{\mathrm{AR}} & \mathbf{T}_{\mathrm{AR}} \end{bmatrix}^{\mathrm{T}}$, $\mathbf{K}_2 = \begin{bmatrix} \mathbf{D}_{\mathrm{BL}} & -\mathbf{T}_{\mathrm{BL}} \end{bmatrix}^{\mathrm{T}}$, $\mathbf{K}_3 = \begin{bmatrix} \mathbf{D}_{\mathrm{AL}} & \mathbf{T}_{\mathrm{AL}} \end{bmatrix}^{\mathrm{T}}$, and $\mathbf{K}_4 = \begin{bmatrix} \mathbf{D}_{\mathrm{BR}} & -\mathbf{T}_{\mathrm{BR}} \end{bmatrix}^{\mathrm{T}}$. The band structure of the periodic bi-layer beam can be determined by solving Equation (11) with the eight roots of the propagation constant.

2.4. Forced Response

A finite periodic bi-layer beam with N cells is shown in Figure 4, where both ends of the beam are set as free boundary conditions. A harmonic force $F_s = F_{s0}\mathrm{e}^{\mathrm{j}\omega t}$ is applied at the left end of the beam.

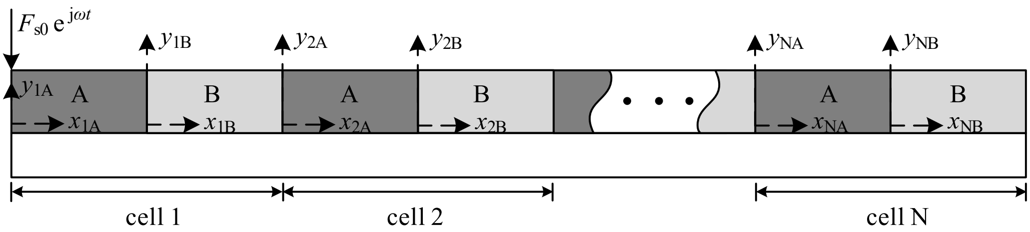

Figure 4. A finite bi-layer beam with the PFLD structure.

According to Equation (7), the generalized displacements and forces at both ends of sub-cell iA and sub-cell iB can be given as follows [26]:

$$\begin{cases} \mathbf{d}_{i\mathrm{AL}} = \mathbf{D}_{i\mathrm{AL}}\boldsymbol{\varphi}_{i\mathrm{A}};\ \mathbf{d}_{i\mathrm{AR}} = \mathbf{D}_{i\mathrm{AR}}\boldsymbol{\varphi}_{i\mathrm{A}};\ \mathbf{t}_{i\mathrm{AL}} = \mathbf{T}_{i\mathrm{AL}}\boldsymbol{\varphi}_{i\mathrm{A}};\ \mathbf{t}_{i\mathrm{AR}} = \mathbf{T}_{i\mathrm{AR}}\boldsymbol{\varphi}_{i\mathrm{A}} \\ \mathbf{d}_{i\mathrm{BL}} = \mathbf{D}_{i\mathrm{BL}}\boldsymbol{\varphi}_{i\mathrm{B}};\ \mathbf{d}_{iBR} = \mathbf{D}_{iBR}\boldsymbol{\varphi}_{i\mathrm{B}};\ \mathbf{t}_{i\mathrm{BL}} = \mathbf{T}_{i\mathrm{BL}}\boldsymbol{\varphi}_{i\mathrm{B}};\ \mathbf{t}_{iBR} = \mathbf{T}_{iBR}\boldsymbol{\varphi}_{i\mathrm{B}} \end{cases}, \tag{12}$$

where $\boldsymbol{\varphi}_{i\mathrm{A}}$ and $\boldsymbol{\varphi}_{i\mathrm{B}}$ are the coefficient vectors of sub-cell iA and sub-cell iB, respectively.

At the interface between sub-cell iA and iB ($x_{i\mathrm{A}} = L_\mathrm{A}$ or $x_{i\mathrm{B}} = 0$) and the interface between sub-cell iB and $(i+1)$A ($x_{i\mathrm{B}} = L_\mathrm{B}$ or $x_{(i+1)\mathrm{A}} = 0$), the generalized displacements and forces satisfy the continuous condition and equilibrium condition, indicating the following:

$$\begin{cases} \mathbf{d}_{i\mathrm{AR}} = \mathbf{d}_{i\mathrm{BL}};\ \mathbf{t}_{i\mathrm{AR}} = -\mathbf{t}_{i\mathrm{BL}} & (i = 1,2,\cdots,N) \\ \mathbf{d}_{i\mathrm{BR}} = \mathbf{d}_{(i+1)\mathrm{AL}};\ \mathbf{t}_{i\mathrm{BR}} = -\mathbf{t}_{(i+1)\mathrm{AL}} & (i = 1,2,\cdots,N-1) \end{cases}. \tag{13}$$

Substituting Equation (12) into Equation (13) yields the following:

$$\begin{cases} \boldsymbol{\varphi}_{i\mathrm{B}} = \mathbf{P}_{\mathrm{AB}}\boldsymbol{\varphi}_{i\mathrm{A}} \\ \boldsymbol{\varphi}_{(i+1)\mathrm{A}} = \mathbf{P}\boldsymbol{\varphi}_{i\mathrm{A}} \end{cases}, \tag{14}$$

where $\mathbf{P}_{\mathrm{AB}} = \mathbf{K}_{i\mathrm{B}}^{-1}\mathbf{K}_{i\mathrm{A}}$ and $\mathbf{P} = \mathbf{H}_{(i+1)\mathrm{A}}^{-1}\mathbf{H}_{i\mathrm{B}}\mathbf{K}_{i\mathrm{B}}^{-1}\mathbf{K}_{i\mathrm{A}}$ in which $\mathbf{K}_{i\mathrm{A}} = \begin{bmatrix}\mathbf{D}_{i\mathrm{AR}} & \mathbf{T}_{i\mathrm{AR}}\end{bmatrix}^\mathrm{T}$, $\mathbf{K}_{i\mathrm{B}} = \begin{bmatrix}\mathbf{D}_{i\mathrm{BR}} & \mathbf{T}_{i\mathrm{BR}}\end{bmatrix}^\mathrm{T}$, $\mathbf{H}_{i\mathrm{B}} = \begin{bmatrix}\mathbf{D}_{i\mathrm{BR}} & \mathbf{T}_{i\mathrm{BR}}\end{bmatrix}^\mathrm{T}$, and $\mathbf{H}_{(i+1)\mathrm{A}} = \begin{bmatrix}\mathbf{D}_{(i+1)\mathrm{AL}} & -\mathbf{T}_{(i+1)\mathrm{AL}}\end{bmatrix}^\mathrm{T}$.

Therefore, $\boldsymbol{\varphi}_{i\mathrm{A}}$ and $\boldsymbol{\varphi}_{i\mathrm{B}}$ can be expressed by $\boldsymbol{\varphi}_{1\mathrm{A}}$ as follows:

$$\begin{cases} \boldsymbol{\varphi}_{i\mathrm{A}} = \mathbf{P}^{i-1}\boldsymbol{\varphi}_{1\mathrm{A}} \\ \boldsymbol{\varphi}_{i\mathrm{B}} = \mathbf{P}_{\mathrm{AB}}\mathbf{P}^{i-1}\boldsymbol{\varphi}_{1\mathrm{A}} \end{cases}. \tag{15}$$

For a finite periodic bi-layer beam with a transverse force applied at the left beam end, the generalized forces at the left and right beam ends can be given as $\mathbf{t}_{1\mathrm{AL}} = \begin{bmatrix}0 & 0 & F_{s0} & 0\end{bmatrix}^\mathrm{T}$ and $\mathbf{t}_{N\mathrm{BR}} = \begin{bmatrix}0 & 0 & 0 & 0\end{bmatrix}^\mathrm{T}$, respectively. As $\boldsymbol{\varphi}_{NB} = \mathbf{P}_{\mathrm{AB}}\mathbf{P}^{N-1}\boldsymbol{\varphi}_{1\mathrm{A}}$, the equations of motion for the finite periodic bi-layer beam can be expressed as follows:

$$\begin{bmatrix} \mathbf{T}_{1\mathrm{AL}} \\ \mathbf{T}_{\mathrm{NBR}}\mathbf{P}_{\mathrm{AB}}\mathbf{P}^{N-1} \end{bmatrix}\boldsymbol{\varphi}_{1\mathrm{A}} = \begin{bmatrix} \mathbf{t}_{1\mathrm{AL}} \\ \mathbf{t}_{\mathrm{NBR}} \end{bmatrix}. \tag{16}$$

From Equation (16), the coefficient $\boldsymbol{\varphi}_{1\mathrm{A}}$ can be calculated. Thus, the coefficient vectors of all the other sub-cells can be determined using Equation (15), and the generalized displacements and forces of all the sub-cells can finally be acquired using Equation (7).

3. Numerical Results

3.1. The Attenuation from the Bragg Scattering

In order to illustrate the flexural wave attenuation performance of the periodic bi-layer beam, both the propagation constant in an infinite periodic structure and the forced vibration response of a finite periodic structure were calculated using the theory proposed in Section 2. The material parameters and dimensions of the unit cell used in the numerical calculation are given in Table 1.

Table 1. The material parameters and dimensions of the unit cell.

	E (GPa)	*G* (GPa)	ρ (kg/m^3)	v	*L* (m)	*b* (m)	*h* (m)
Free layer A	0.186	0.062	900	0.499	0.2	0.02	0.005
Free layer B	86.9	35.6	2460	0.220	0.2	0.02	0.005
Base layer	77.6	28.7	2730	0.352	0.4	0.02	0.002

The damping of the base layer and the two free layers was first set to zero to illustrate the attenuation performance induced by the Bragg scattering. The flexural wave-propagation constants are shown in Figure 5. As shown in the figure, three band gaps showed up in the frequency range 0–650 Hz, namely 26.0–43.8 Hz, 121.4–233.1 Hz, and 339.0–498.9 Hz, as shown in the gray-shaded regions. As calculated, the band-gap widths of the three band gaps were 17.8 Hz, 111.7 Hz, and 159.9 Hz, with a total bandwidth of 289.4 Hz. The total band-gap ratio reached 44.5% in the frequency range of interest (from 0 Hz to 650 Hz), indicating that nearly half of all flexural waves below 650 Hz could be attenuated.

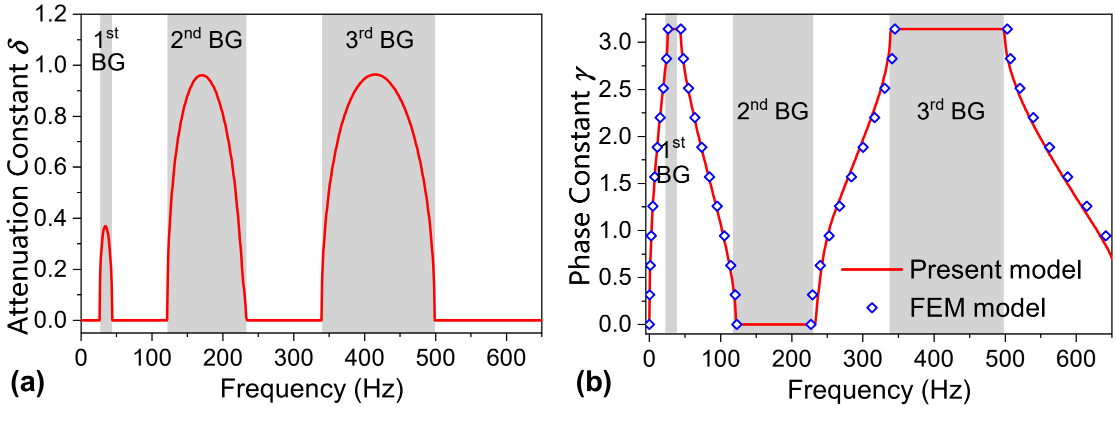

Figure 5. The propagation constants of the infinite bi-layer beam with an undamped PFLD structure: (**a**) decay constant and (**b**) phase constant.

In order to validate the correctness of the model, the flexural-wave phase constant was also calculated using the finite-element method (FEM) with COMSOL-Multiphysics software (Version 5.2). A single-cell geometry, as shown in Figure 3, was meshed with a hexahedral element type, and there were 8000 elements in the model. The meshing resolution was far more adequate for the frequency range considered in this work (0–650 Hz). The Bloch periodic boundary condition was applied at both ends of the cell. Through parametric frequency sweep analysis and characteristic frequency analysis, the phase constant could finally be determined.

The comparison results given in Figure 5b show that the model had excellent agreement with the FEM, which validated the accuracy of the theoretical model.

The vibration response of the finite periodic undamped bi-layer beam with five unit cells was then further examined. A unit harmonic force was applied at the left end of the periodic beam, and the normalized acceleration level at the right end was used to assess the flexural-wave attenuation and propagation performance, which was defined as $20\log_{10}\left(\frac{a}{a_{\mathrm{ref}}F_{s0}}\right)$, where a is the acceleration, $a_{\mathrm{ref}} = 10^{-6}\ \mathrm{ms}^{-2}$ is the referenced acceleration, and F_{s0} is the applied force.

As shown in Figure 6, three vibration-response valleys depicted in gray can be observed, and their frequency bands matched well with the band gaps of the infinite periodic beam shown in Figure 5. The forced vibration calculation model given in this research was also validated by the FEM, as shown in Figure 6. From the above analysis, it can be seen that the periodic bi-layer beam had good filtering characteristics for flexural waves. When damping was not considered, the propagation of flexural waves within the band gaps was suppressed, while the waves outside the band gaps could be smoothly transmitted from the left end to the right end of the beam.

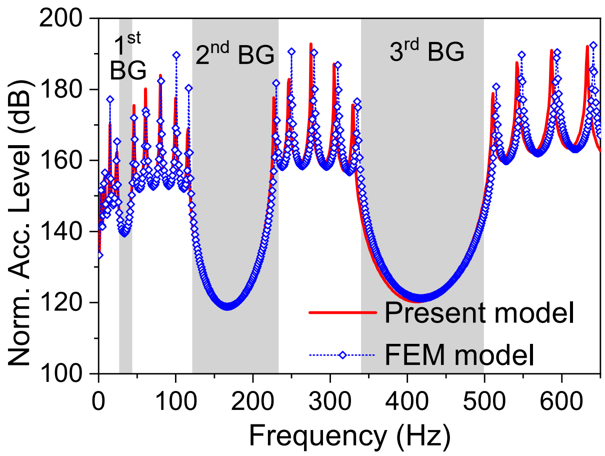

Figure 6. Vibration response at the right end of the finite periodic bi-layer beam (the gray-shaded regions indicate the band gaps of the infinite periodic bi-layer beam).

3.2. The Combined Effects of the Bragg Scattering and Damping

For the bi-layer beam with an undamped PFLD structure, the vibration in the band gaps could be significantly attenuated while the waves in the passbands continued to smoothly propagate. In order to further reduce the overall vibration, the damping of free layers was considered. The concept of a complex modulus was used in the analysis to assess the damping effects. Thus, the Young's modulus of the material could be given as $E = E_s(1 + j\eta)$, where E_s and η represent the storage modulus and damping loss factor, respectively.

In the following analysis, the base layer and free layer B were used with an elastic material where damping was not considered, and the free layer A was used with a viscoelastic damping material, with the damping loss factor represented by η_A. The material and geometric parameters remained consistent with the values in Table 1, except for the loss factor parameters. Figure 7 shows the attenuation constants of the infinite periodic structures and the vibration responses of the right end of the finite periodic structures, with the various damping loss factors of free layer A.

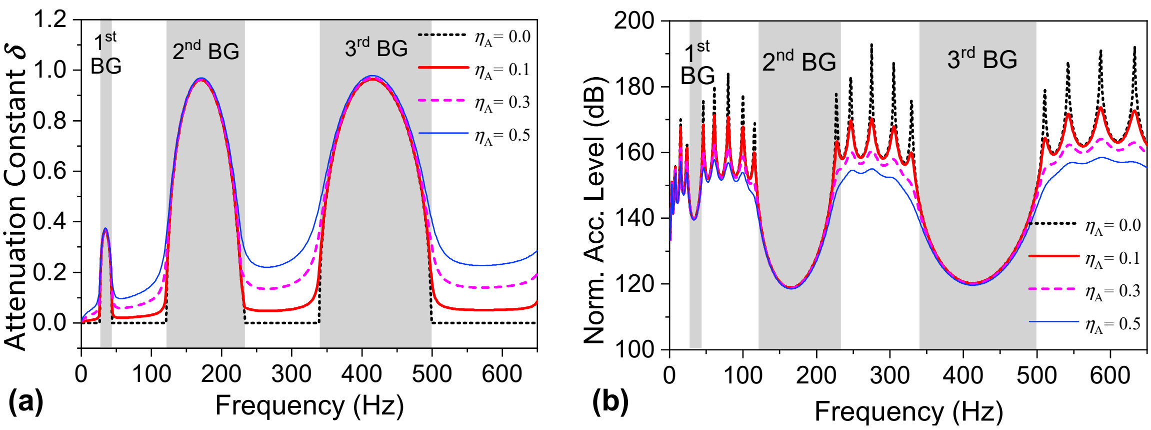

Figure 7. (**a**) The decay constants of the infinite periodic bi-layer beam and (**b**) the vibration responses of the finite periodic bi-layer beam.

As shown in Figure 7a, within the band gaps, the attenuation constant slightly increased with the increase in the loss factors, and the effects of the damping loss factors could be ignored. Outside the band gaps, the free layer's damping loss factor significantly affected the attenuation constants. One of the main reasons for the weak effect of the damping on the attenuation constants in the band gaps can be stated as follows: the band-gap generation mechanism in the periodic bi-layer beam was the Bragg scattering. In the band-gap frequency range, the incident wave was strongly reflected because of periodicity. Thus, in the wave-propagation process, the reflected wave carried most of the energy; however, the transmitted wave carried very little energy. The effect of material damping is to dissipate the energy of transmitted wave energy along the foregoing wave-propagation direction. As the transmitted wave energy was very little, the effect of the damping on the vibration reduction was quite weak in the band gap. However, out of the band-gap frequency range, the transmitted wave carried most of the energy, and the damping could significantly affect the attenuation constant.

When η_A was equal to zero, the attenuation constant in the passbands was zero, meaning that the flexural wave freely propagated without attenuation. As the value of η_A increased, the attenuation constants outside the band gaps also gradually increased; thus, the ability to suppress flexural waves was gradually strengthened. The vibration response of the finite period bi-layer beam shown in Figure 7b also showed that after considering the damping effect of the free layer, an excellent flexural wave suppression effect was also achieved outside the band gap.

From the above analysis, it can be seen that when damping was introduced into the free layer, the attenuation of the flexural waves within the band gaps was mainly controlled by the Bragg scattering effect, and outside the band gaps, it was mainly controlled by the damping dissipation effect. The combined effect of the above two effects enabled the structure to achieve good vibration suppression effects throughout the entire broadband range, both within and outside of the band gaps.

3.3. Parametric Analysis

The effects of the dimensional parameters on the band-gap location f, band-gap width f_b, decay level L_{δ_f}, and vibration response were examined. The parameters of the periodic bi-layer beam were set as shown in Table 1, and the total length of the finite periodic bi-layer was 2.0 m. The above parameters remained unchanged unless otherwise stated.

The effects of the cell length L on the band-gap properties were first considered, with the length L varying from 0.1 m to 1 m, and $L_A = L_B$. As shown in Figure 8, with the increases in L, the band-gap locations, band-gap widths, and decay levels decreased for both the first and second band gaps. Thus, a large cell length was advantageous for reducing lower-frequency vibrations. However, increasing the cell lengths led to reduced band-gap widths and decay levels. Therefore, cell length should be appropriately designed to suppress vibrations at a targeted frequency, with sufficient band-gap widths and decay levels.

The effects of the sub-cell-length ratio $\alpha = L_A/L_B$ on the band-gap properties were also considered, where sub-cell A corresponded to a low-modulus and low-density material, and sub-cell B corresponded to a high-modulus and high-density material. In this parametric analysis, the parameter α varied from 0.1 to 10, with $L = 0.4$ m (remaining unchanged). As shown in Figure 9, with the increases in α, the band-gap locations, band-gap widths, and decay levels generally decreased for the first band gap. However, the variation trends became more complicated for the second band gap. As shown in Figure 9b,c, both the band-gap width and decay level for the second band gap first decreased and then increased, and they finally decreased with increasing α values, reaching their maximum values of 189.8 Hz and 16.6 dB at $\alpha = 0.5$ and $\alpha = 0.8$, respectively. Thus, designing the sub-cell-length ratio values as the above two values was advantageous for better vibration attenuation performance in the band gap. As the attenuation out of the band gaps mainly came from the damping dissipation by the free layer material of sub-cell A, we determined that the value of α should not be too small. Otherwise, the vibration out of the band gaps would not be acceptably suppressed. As shown in Figure 9d, for the case where $\alpha = 0.2$, although the first band-gap frequency was very low, the bandwidth was wide and the vibration suppression ability in the band gap was strong, and so vibrations in the frequency range 150–450 Hz were considerable. The overall attenuation performance in the case where $\alpha = 0.2$ was inferior to that of the case where $\alpha = 1$. Therefore, the sub-cell-length ratio should be set to a moderate value to obtain better vibration suppression both inside and outside of the band gap.

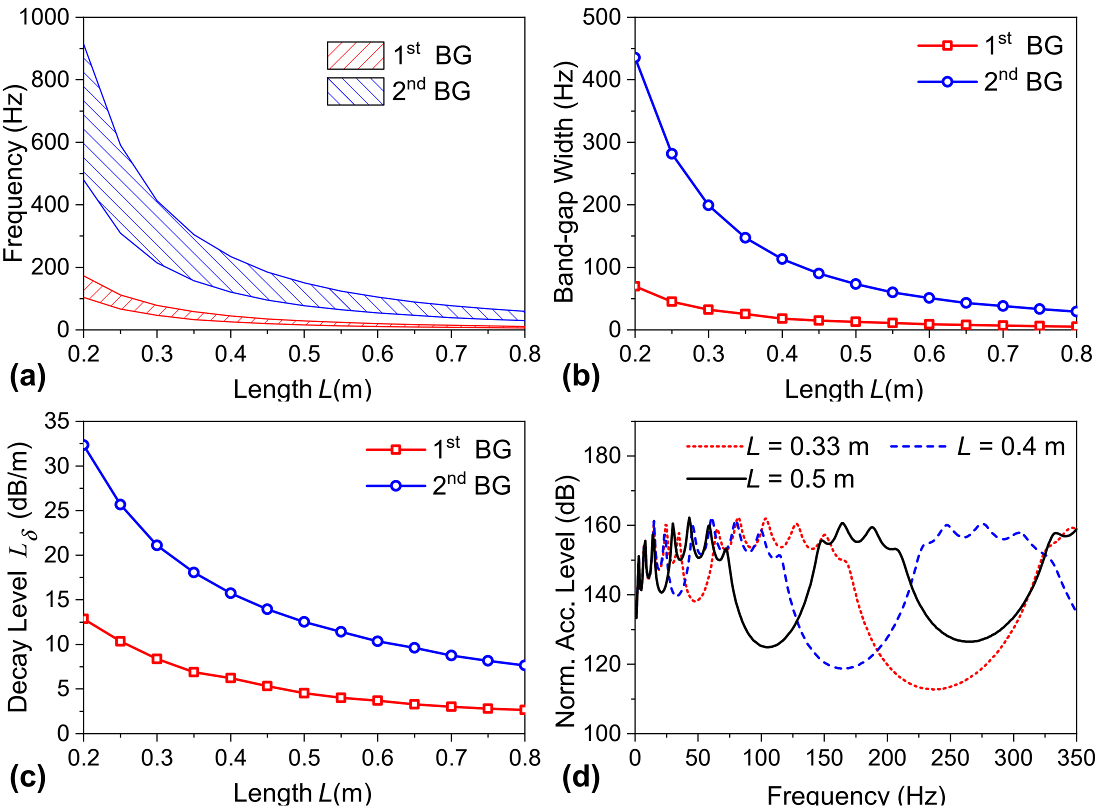

Figure 8. The effects of the cell length L on the (**a**) band-gap locations, (**b**) band-gap widths, (**c**) decay levels, and (**d**) vibration responses.

The effects of the thickness ratio $\beta = h_2/h_1$ on the band-gap properties are shown in Figure 10, where the base layer's thickness remained unchanged at $h_1 = 2$ mm.

As shown in Figure 10a, with the increases in β, the band-gap starting frequencies of the two band gaps gently varied, while the band-gap cutoff frequencies gradually increased, resulting in the band-gap widths increasing with the increasing thickness ratio β (Figure 10b). The increase in β was also beneficial for obtaining strong attenuation abilities in the band gaps, as shown in Figure 10c. It can also be obtained from Figure 10d that when the thickness ratio was increased, the vibration suppression effect both inside and outside of the band gap would be enhanced. The enhancement inside the band gap was caused by the increased effective modulus and the density difference between sub-cell A and sub-cell B, resulting in increased Bragg scattering. In comparison, the enhancement outside of the band gap was caused by the increased energy dissipation induced by the free layer's damping. It can be seen from the above analysis that when designing a periodic bi-layer beam, the thickness ratio should be designed with a value that is as large as practical engineering will allow.

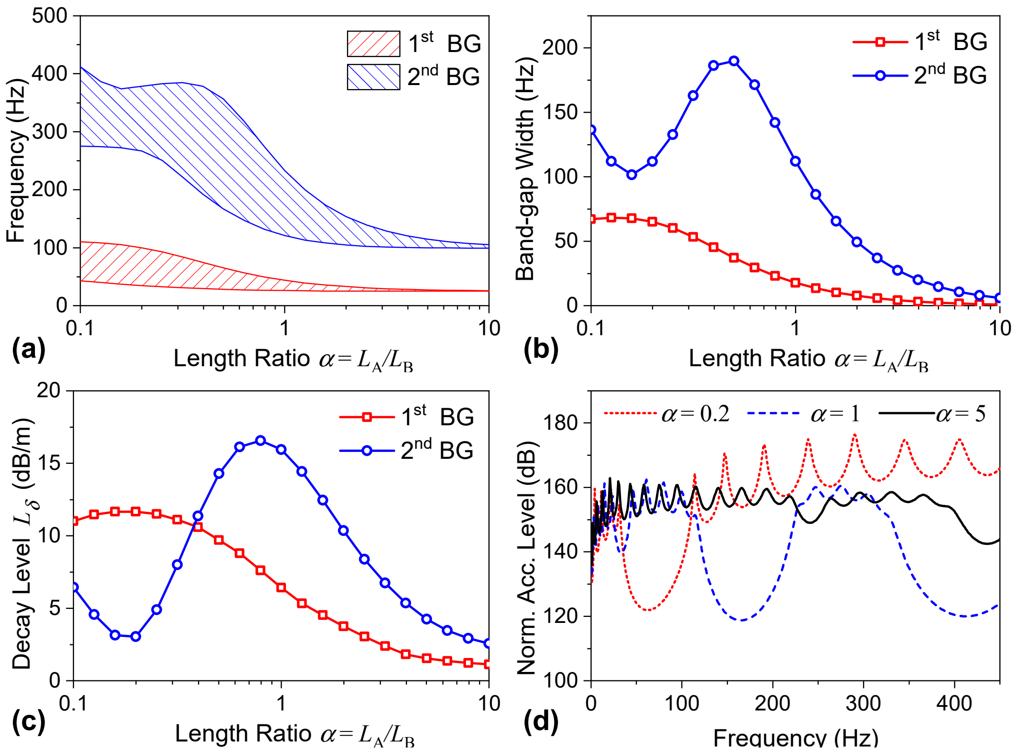

Figure 9. The effects of the sub-cell-length ratio $\alpha = L_a/L_B$ on the (**a**) band-gap locations, (**b**) band-gap widths, (**c**) decay levels, and (**d**) vibration responses.

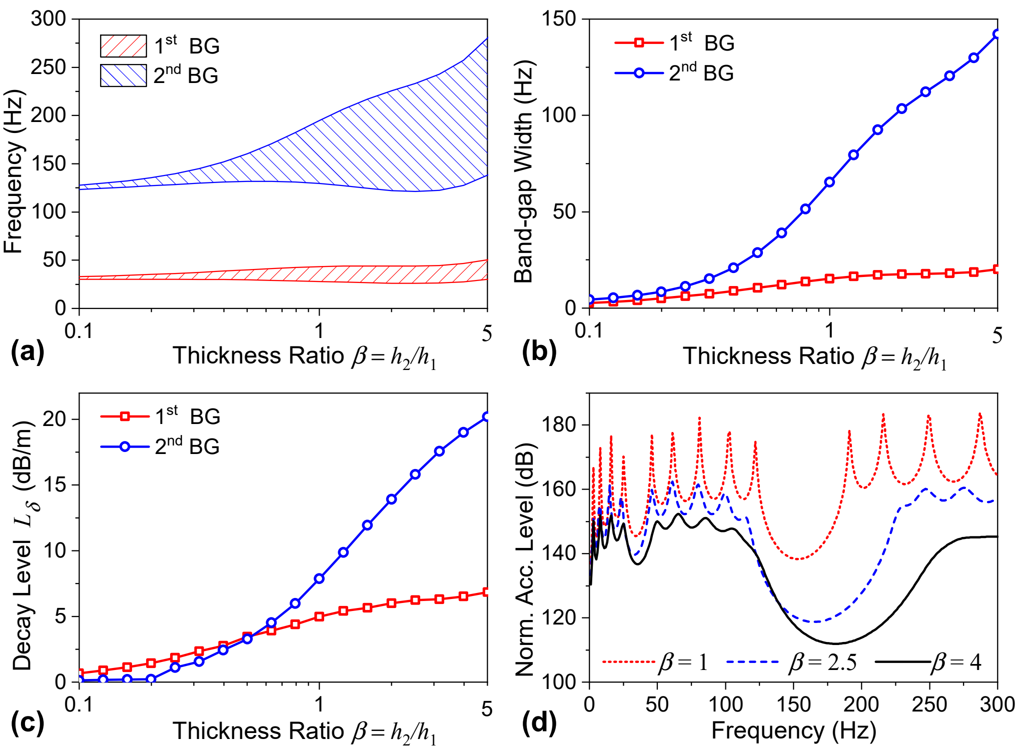

Figure 10. The effects of the thickness ratio $\beta = h_2/h_1$ on the (**a**) band-gap locations, (**b**) band-gap widths, (**c**) decay levels, and (**d**) vibration responses.

4. Experiment Verification

In order to verify the analytical model and the practical attenuation performance, a periodic bi-layer beam specimen, as shown in Figure 11, was fabricated and tested. The base layer of the specimen was made of aluminum, and the periodic free layers were made of polymer rubber (PMRB) and polymethyl methacrylate (PMMA). The specimen consisted of eight cells, where the single units are as shown in Figure 12. For each cell, sub-cell A and sub-cell B had identical dimensions, with lengths of 100 mm, widths of 50 mm, base layer thicknesses of 1.85 mm, and free layer thicknesses of 5 mm.

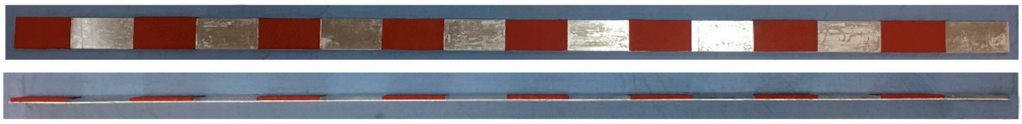

Figure 11. The tested periodic bi-layer beam specimen.

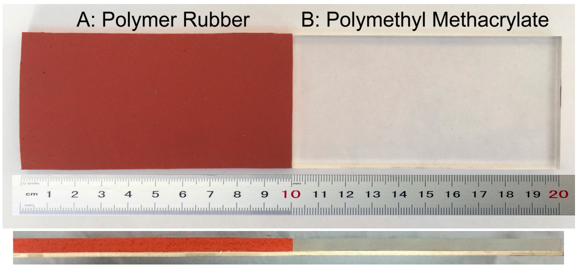

Figure 12. A single unit of the periodic bi-layer beam.

The densities of the aluminum, PMRB, and PMMA were measured as 2690.6 kg/m^3, 984.0 kg/m^3, and 1153.1 kg/m^3, respectively. The Young's modulus and the loss factor of the aluminum were set as 77.6 GPa and 0.001, respectively, while those of the PMRB and PMMA were tested in an experiment, as shown in Figure 13.

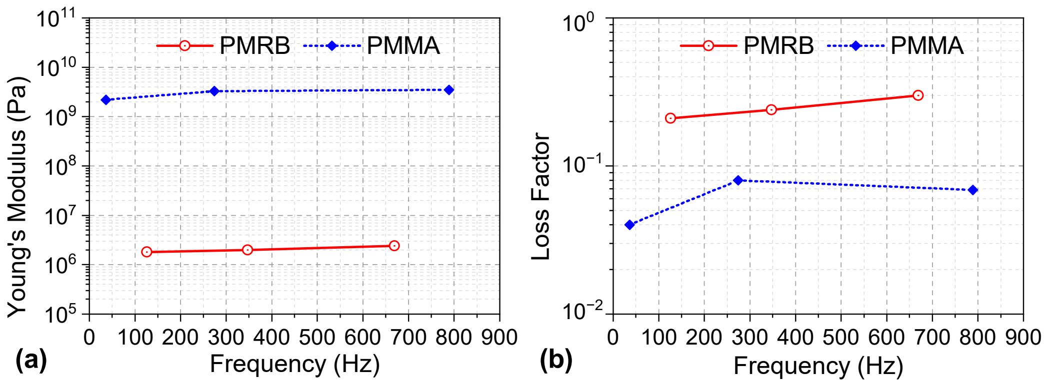

Figure 13. Test results of the polymer rubber (PMRB) and polymethyl methacrylate (PMMA) for the (**a**) Young's moduli and (**b**) loss factors.

The experimental schematic diagram and the practical experimental setup are shown in Figures 14 and 15, respectively. The specimen was suspended by two elastic ropes. The signal generator and analyzer (B&K 3560B) generated an excitation signal, which was transmitted to a vibration exciter (JZ 2A) through a power amplifier (B&K 2716). In order to obtain the normalized vibration response and then compare it to the analytical model, the input acceleration and input force signals were acquired using an impedance head (B&K 8001), which was mounted on the exciter. These two signals were analyzed using a signal analyzer (B&K 3050A) after the corresponding charge signals were amplified and transformed to voltage signals by a charger amplifier (B&K 2692). The input force was used as a reference signal during the post-data analysis. The excitation position was located at the left beam end to better study the vibration transmission performance. The vibration responses of the specimen were acquired using eight acceleration sensors (PCB

M353B16), with each of the two neighboring sensors' spaces set at approximately 20 cm. These acceleration signals were first transmitted to the signal conditioners (PCB 482A22) and then to the signal analyzers (B&K 3050A). The experimental data were finally processed by the testing software in the testing computer.

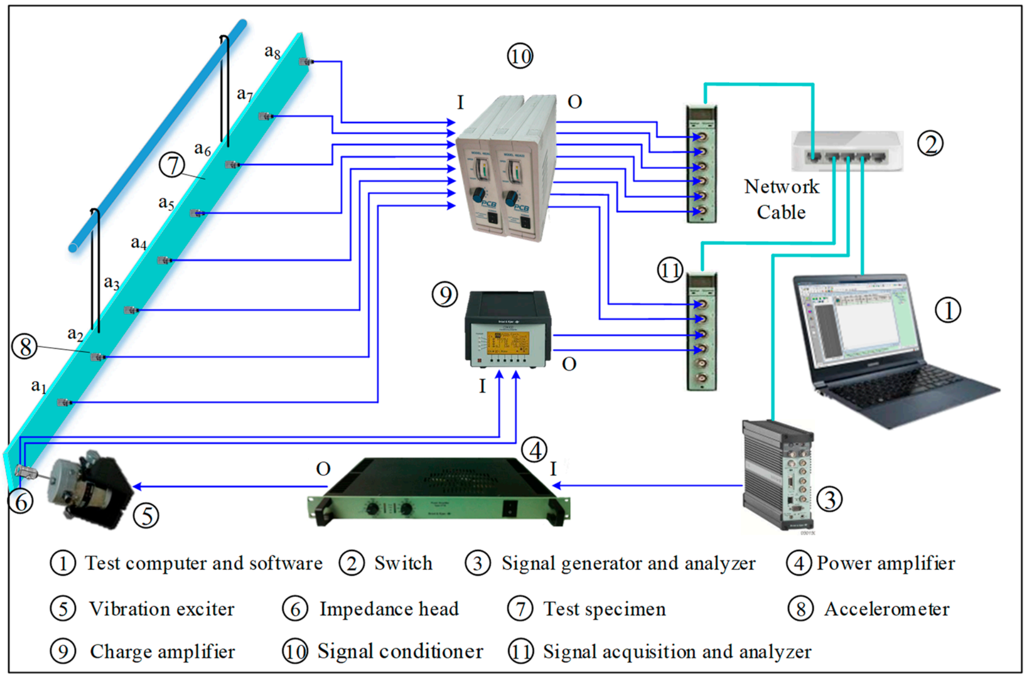

Figure 14. Schematic diagram of the experimental setup.

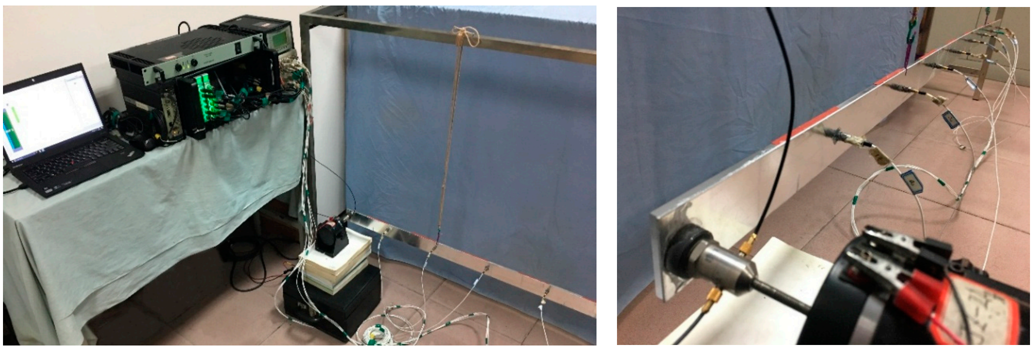

Figure 15. Practical experimental setup.

The acceleration acquired from each accelerometer was normalized by the input force. The normalized accelerations at the excitation end and at the opposite end of the specimen are given in Figure 16. As shown in the figure, in the frequency ranges of approximately 65–103 Hz and 340–540 Hz, the periodic bi-layer beam provided band-gap attenuation performances where vibrations were significantly compressed for the tail end. The normalized accelerations from the experiment and the present theory are further compared in Figure 17. As shown in the figure, the experimental results' levels and varying trends matched well with the theoretical results in the overall frequency range, except for some specific frequencies, which validated the effectiveness of the theory. The band-gap frequency results calculated from the present theory were slightly larger than those obtained from the experiment. The differences may have been induced by the specimen's glue between the base and free layers, which was not considered in the theoretical model.

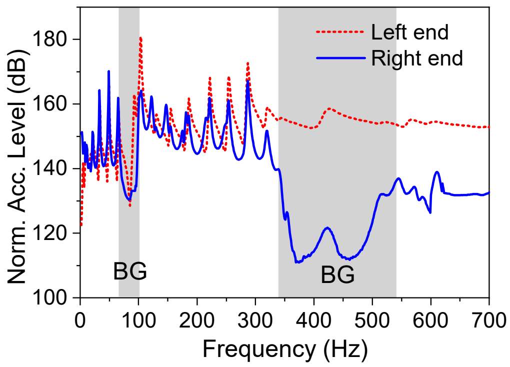

Figure 16. The normalized accelerations at the left and right ends of the beam in the experiment (BG, band gap).

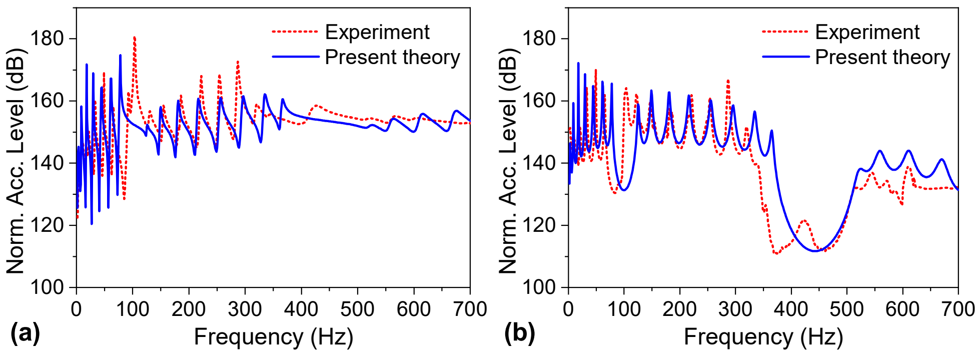

Figure 17. Comparisons of the experiment and the theory for the normalized accelerations (**a**) at the left and (**b**) at the right ends of the beam.

The vibration responses tested by the other acceleration sensors are also given in Figure 18, where the transmission characteristics along the axial direction at two specific frequencies were further studied. As shown in the figure, for the frequency 450 Hz, located in the band gap, the vibrations were significantly attenuated along the direction of the wave propagation, with a decay rate of approximately 27.5 dB/m. This attenuation was caused by both the Bragg scattering and the damping. For the frequency 287 Hz, located out of the band gap, the vibrations along the axial direction performed as fluctuations, with the envelope's magnitude decreasing with the direction of the wave propagation. This attenuation was mainly caused by the damping.

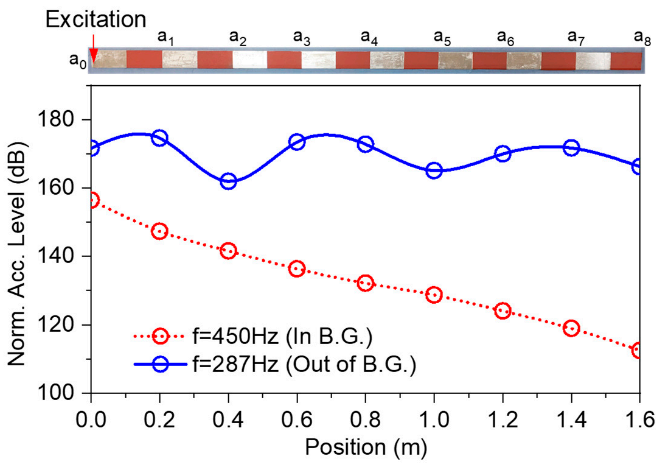

Figure 18. Transmission characteristics of the periodic beam in the band gap (450 Hz) and out of the band gap (287 Hz) (B.G., band gap).

In order to further illustrate the attenuation performance of the periodic bi-layer beam, the other three specimens shown in Figure 19 (specimens #2, #3, and #4) were also fabricated and tested for comparison purposes. Specimen #1 was the already considered periodic bi-layer beam. Specimens #2 and #3 were uniform bi-layer beams, with the free layers made of purely PMMA and polymer rubber, respectively. Specimen #4 was a single-layer aluminum-made uniform beam of the same weight as the periodic bi-layer beam.

(**a**) Overhead view (**b**) Side view

Figure 19. The four tested specimens of the periodic/uniform bi-layer beams and the single-layer uniform beam.

The comparison results are shown in Figure 20. As shown in the figure, the vibration responses of the four tested specimens were comparable in the low-frequency range. In the high-frequency range, the vibrations of specimens #1, #2, and #3 were lower than those of specimen #4 owing to the damping dissipation effects.

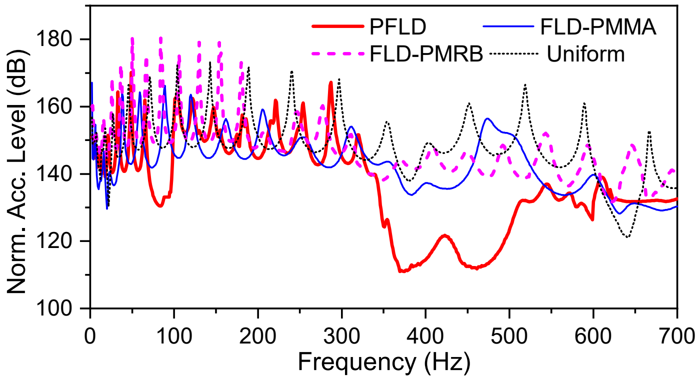

Figure 20. The experimental comparison results of the four specimens for the normalized accelerations at the right end of the beam.

It may seem unreasonable that the vibrations in the FLD-PMRB case were larger than those of the uniform case. One of the main reasons may be stated as follows: the uniform case's aluminum beam thickness was set at approximately 3.8 mm, which was larger than the FLD-PMRB case's base layer thickness of 1.85 mm, resulting in the uniform case's bending rigidity being potentially larger than that of the FLD-PMRB case. In addition, the Young's modulus of the damping layer in the FLD-PMRB case was very small (approximately 0.002 GPa), which was quite small compared with that of the aluminum base layer (76 GPa). In addition, at the lower frequencies, it was harder to dissipate energy through the free layer's damping because of the large wavelength. Therefore, the vibrations of the FLD-PMRB case were potentially larger than those of the uniform case at the lower frequencies. As shown in Figure 20, with the increases in frequency, the damping dissipation ability gradually increased, and the FLD-PMRB case's response became smaller than that of the uniform case by approximately 200 Hz.

As shown in Figure 20, in the band-gap frequency range, the vibrations of the periodic bi-layer beam were significantly reduced compared with those of the other three specimens, with an average attenuation of approximately 20 dB. Thus, the PFLD treatment was beneficial for improving the attenuation performance of the beam structure.

5. Conclusions

Periodicity was introduced into a damping treatment to improve vibration reduction performance, and the concept of a periodic free-layer damping (PFLD) treatment was proposed in this study. The theoretical models of the periodic bi-layer beam's band structure and the forced response were established using the Hamilton principle and transfer matrix method. The accuracy of the theoretical model was verified by the finite-element method, showing that the analytical results matched well with the numerical simulation results.

When a viscoelastic damping material was used in a free layer of the periodic bi-layer composite beam, the flexural wave attenuation of the structure was mainly caused by the Bragg scattering effect, and the energy dissipation effect was caused by the damping. Bragg scattering played a dominant role in the band gaps, and energy dissipation played a dominant role outside the band gaps. The combined effect of the two mechanisms enabled effective control of the propagation of the waves within and outside of the band gaps in the low-frequency range.

The dimensional parameters of the periodic bi-layer beam significantly affected the overall vibration reduction performance. Increasing cell lengths was beneficial for moving the band gap toward lower frequencies, but at the same time, the widths of the band gaps and the ability to suppress vibrations within the band gaps decreased. The sub-cell-length ratios should be carefully designed with moderate values to balance the effect of the Bragg scattering and the damping dissipation to achieve better performances both inside and outside of the band gaps. Under actual conditions, the greater the thickness ratio was between the free and base layers, the more favorable it was for structural vibration suppression.

The experiment results showed that the PFLD treatment can increase vibration reduction levels in the low-frequency band gaps compared with a traditional FLD treatment. This work was limited to a bi-layer beam structure with a PFLD treatment. An extension to a plate or shell structure is possible and may provide more direct guidance for controlling vibrations in practical structures.

Author Contributions: Conceptualization, Z.G. and M.S.; methodology, Z.G.; software, Z.G.; validation, Z.G. and H.Z.; formal analysis, Z.G.; investigation, Z.G.; resources, Z.G. and M.S.; data curation, H.Z.; writing—original draft preparation, Z.G.; writing—review and editing, M.S. and H.Z.; visualization, Z.G.; supervision, M.S.; project administration, M.S.; funding acquisition, Z.G. and M.S. All authors have read and agreed to the published version of the manuscript.

Funding: This research was funded by the National Natural Science Foundation of China (grant number 52301388), Ningbo Natural Science Foundation (grant number 2021J057), and the Natural Science Foundation of Shannxi Province, China (grant number 2021JLM-39). The APC was funded by the National Natural Science Foundation of China (grant number 52301388).

Institutional Review Board Statement: Not applicable.

Data Availability Statement: The data presented in this study are available in the article.

Acknowledgments: The authors gratefully acknowledge the experimental help from Yiwei Yin.

Conflicts of Interest: The authors declare no conflict of interest.

Appendix A

The coefficients a_{ij} in Equations (3) and (4) are expressed as follows:

$$a_{11} = k_1 A_1 G_1, \tag{A1}$$

$$a_{12} = k_2 A_2 G_2, \tag{A2}$$

$$a_{13} = -\omega^2 \sum_{i=1}^{3} \rho_i A_i, \tag{A3}$$

$$a_{14} = -a_{11} - a_{12}, \tag{A4}$$

$$a_{21} = \omega^2 \rho_1 A_1 + \omega^2 \rho_2 A_2, \tag{A5}$$

$$a_{22} = E_1 A_1 + E_2 A_2, \tag{A6}$$

$$a_{23} = h_1 \rho_2 A_2 \omega^2 / 2, \tag{A7}$$

$$a_{24} = h_1 E_2 A_2 / 2, \tag{A8}$$

$$a_{25} = h_2 \rho_2 A_2 \omega^2 / 2, \tag{A9}$$

$$a_{26} = h_2 E_2 A_2 / 2, \tag{A10}$$

$$a_{31} = a_{23}, \tag{A11}$$

$$a_{32} = a_{24}, \tag{A12}$$

$$a_{33} = \omega^2 \rho_1 I_1 + \omega^2 h_1^2 \rho_2 A_2 / 4 - a_{11}, \tag{A13}$$

$$a_{34} = E_1 I_1 + h_1^2 E_2 A_2 / 4, \tag{A14}$$

$$a_{35} = \omega^2 \rho_2 I_2 + \omega^2 h_2^2 \rho_2 A_2 / 4, \tag{A15}$$

$$a_{36} = h_1 h_2 E_2 A_2 / 4, \tag{A16}$$

$$a_{37} = a_{11}, \tag{A17}$$

$$a_{41} = a_{25}, \tag{A18}$$

$$a_{42} = a_{26}, \tag{A19}$$

$$a_{43} = \omega^2 h_1 h_2 \rho_2 A_2 / 4, \tag{A20}$$

$$a_{44} = h_1 h_2 E_2 A_2 / 4, \tag{A21}$$

$$a_{45} = a_{35} - a_{12}, \tag{A22}$$

$$a_{46} = E_2 I_2 + h_2^2 E_2 A_2 / 4, \text{ and} \tag{A23}$$

$$a_{47} = a_{12}. \tag{A24}$$

The matrices $\mathbf{D}(x)$ in Equation (7) are expressed as follows:

$$\mathbf{D}(x) = \begin{bmatrix} d_{11}e^{r_1 x} & d_{12}e^{r_2 x} & \cdots & d_{18}e^{r_8 x} \\ d_{21}e^{r_1 x} & d_{22}e^{r_2 x} & \cdots & d_{28}e^{r_8 x} \\ d_{31}e^{r_1 x} & d_{32}e^{r_2 x} & \cdots & d_{38}e^{r_8 x} \\ d_{41}e^{r_1 x} & d_{42}e^{r_2 x} & \cdots & d_{48}e^{r_8 x} \end{bmatrix}, \tag{A25}$$

where $d_{1j} = \frac{|[\mathbf{v}_4, \mathbf{v}_2, \mathbf{v}_3]|}{|[\mathbf{v}_1, \mathbf{v}_2, \mathbf{v}_3]|}$, $d_{2j} = \frac{|[\mathbf{v}_1, \mathbf{v}_4, \mathbf{v}_3]|}{|[\mathbf{v}_1, \mathbf{v}_2, \mathbf{v}_3]|}$, $d_{3j} = \frac{|[\mathbf{v}_1, \mathbf{v}_2, \mathbf{v}_4]|}{|[\mathbf{v}_1, \mathbf{v}_2, \mathbf{v}_3]|}$, and $d_{4j} = 1$, and the vectors $\mathbf{v}_i$ are given as follows:

$$\begin{cases} \mathbf{v}_i = \left[a_{2(2i-1)} + a_{2(2i)}\lambda_j^2,\ a_{3(2i-1)} + a_{3(2i)}\lambda_j^2,\ a_{4(2i-1)} + a_{4(2i)}\lambda_j^2\right]^{\mathrm{T}} \quad (i = 1, 2, 3) \\ \mathbf{v}_4 = \left[0, -a_{37}\lambda_j, -a_{47}\lambda_j\right]^{\mathrm{T}} \end{cases}. \tag{A26}$$

The matrices $\mathbf{T}(x)$ in Equation (7) are expressed as follows:

$$\mathbf{T}(x) = \begin{bmatrix} t_{11}e^{r_1 x} & t_{12}e^{r_2 x} & \cdots & t_{18}e^{r_8 x} \\ t_{21}e^{r_1 x} & t_{22}e^{r_2 x} & \cdots & t_{28}e^{r_8 x} \\ t_{31}e^{r_1 x} & t_{32}e^{r_2 x} & \cdots & t_{38}e^{r_8 x} \\ t_{41}e^{r_1 x} & t_{42}e^{r_2 x} & \cdots & t_{48}e^{r_8 x} \end{bmatrix}, \tag{A27}$$

where the coefficients t_{ij} can be expressed as follows:

$$t_{1j} = a_{22}r_j d_{1j} + a_{24}r_j d_{2j} + a_{26}r_j d_{3j}, \tag{A28}$$

$$t_{2j} = a_{24}r_j d_{1j} + a_{34}r_j d_{2j} + a_{36}r_j d_{3j}, \tag{A29}$$

$$t_{3j} = a_{26}r_j d_{1j} + a_{36}r_j d_{2j} + a_{46}r_j d_{3j},\ \text{and} \tag{A30}$$

$$t_{4j} = -a_{11}d_{2j} - a_{12}d_{3j} + (a_{11} + a_{12})r_j \tag{A31}$$

References

1. Ungar, E.E.; Kerwin, E.M. Plate damping due to thickness deformations in attached viscoelastic layers. *J. Acoust. Soc. Am.* **1964**, *36*, 386–392. [CrossRef]
2. Roy, P.K.; Ganesan, N. Dynamic studies on beams with unconstrained layer damping treatment. *J. Sound Vib.* **1996**, *195*, 417–427. [CrossRef]
3. Cortés, F.; Elejabarrieta, M.J. Structural vibration of flexural beams with thick unconstrained layer damping. *Int. J. Solids Struct.* **2008**, *45*, 5805–5813. [CrossRef]
4. Kerwin, E.M. Damping of flexural waves by a constrained viscoelastic layer. *J. Acoust. Soc. Am.* **1959**, *31*, 952–962. [CrossRef]
5. Teng, T.L.; Hu, N.K. Analysis of damping characteristics for viscoelastic laminated beams. *Comput. Methods Appl. Mech. Eng.* **2001**, *190*, 3881–3892. [CrossRef]
6. Kumar, A.; Panda, S. Design of a 1-3 viscoelastic composite layer for improved free/constrained layer passive damping treatment of structural vibration. *Compos. Part B Eng.* **2016**, *96*, 204–214. [CrossRef]
7. Rao, M.D. Recent applications of viscoelastic damping for noise control in automobiles and commercial airplanes. *J. Sound Vib.* **2003**, *262*, 457–474. [CrossRef]
8. Roland, C.M. Naval applications of elastomers. *Rubber Chem. Technol.* **2004**, *77*, 542–551. [CrossRef]
9. Gallimore, C.A. Passive Viscoelastic Constrained Layer Damping Application for a Small Aircraft Landing Gear System. Master's Thesis, Virginia Polytechnic Institute and State University, Blacksburg, VA, USA, 2008.
10. Oberst, H.; Frankenfeld, K. Damping of the bending vibrations of thin laminated metal beams connected through adherent layer. *Acustica* **1952**, *2*, 181–194.
11. Sheng, M.; Wang, M.; Ma, J. *Fundamentals of Noise and Vibration Control Technology*; Science Press: Beijing, China, 2017.
12. Hu, Y.C.; Huang, S.C. The frequency response and damping effect of three-layer thin shell with viscoelastic core. *Comput. Struct.* **2000**, *76*, 577–591. [CrossRef]

13. Lia, L.; Liao, W.H.; Zhang, D.G.; Guo, Y.B. Vibration analysis of a free moving thin plate with fully covered active constrained layer damping treatment. *Compos. Struct.* **2020**, *235*, 111742. [CrossRef]
14. Tao, W.Z.; Jiang, F.; Li, L.; Zhang, D.G.; Guo, X.; Liao, W.H. Dynamical analysis and vibration estimation of a flexible plate with enhanced active constrained layer damping treatment by combinatorial neural networks of surrogates. *Aerosp. Sci. Technol.* **2023**, *133*, 108136. [CrossRef]
15. Gao, N.S.; Zhang, Z.C.; Deng, J.; Guo, X.Y.; Cheng, B.Z.; Hou, H. Acoustic metamaterials for noise reduction: A review. *Adv. Mater. Technol.* **2022**, *7*, 2100698. [CrossRef]
16. Liao, G.X.; Luan, C.C.; Wang, Z.W.; Liu, J.P.; Yao, X.H.; Fu, J.Z. Acoustic metamaterials: A review of theories, structures, fabrication approaches, and applications. *Adv. Mater. Technol.* **2021**, *6*, 2000787. [CrossRef]
17. Liu, J.Y.; Guo, H.B.; Wang, T. A review of acoustic metamaterials and phononic crystals. *Crystals* **2020**, *10*, 305. [CrossRef]
18. Kushwaha, M.S.; Halevi, P.; Dobrzynski, L.; Djafarirouhani, B. Acoustic band-structure of periodic elastic composites. *Phys. Rev. Lett.* **1993**, *71*, 2022–2025. [CrossRef]
19. Liu, Z.; Zhang, X.; Mao, Y.; Zhu, Y.Y.; Yang, Z.; Chan, C.T.; Sheng, P. Locally resonant sonic materials. *Science* **2000**, *289*, 1734–1736. [CrossRef]
20. Wen, J.; Yu, D.; Wang, G.; Zhao, H.; Liu, Y. Elastic wave band gaps in flexural vibrations of straight beams. *Chin. J. Mech. Eng.* **2005**, *41*, 1–6. [CrossRef]
21. Guo, Z.W.; Sheng, M.P.; Pan, J. Effect of boundary conditions on the band-gap properties of flexural waves in a periodic compound plate. *J. Sound Vib.* **2017**, *395*, 102–126. [CrossRef]
22. Dou, Y.; Zhang, J.; Hu, Y.; Wen, X.; Xia, X.; Zang, M. Numerical and experimental analysis of the stiffness and band-gap properties of shell structures with periodically variable cross sections. *Heliyon* **2023**, *9*, 14191. [CrossRef]
23. Mangaraju, V.; Sonti, V.R. Wave attenuation in periodic three-layered beams: Analytical and FEM study. *J. Sound Vib.* **2004**, *276*, 541–570. [CrossRef]
24. Yeh, J.Y.; Chen, L.W. Wave propagations of a periodic sandwich beam by FEM and the transfer matrix method. *Compos. Struct.* **2006**, *73*, 53–60. [CrossRef]
25. Tian, F. Research on Vibration and Acoustic of Two-Dimensional Periodically Distributed Bulk-Damping. Master's Thesis, Hubei University of Technology, Hubei, China, 2014.
26. Guo, Z.W.; Sheng, M.P. Bandgap of flexural wave in periodic bi-layer beam. *J. Vib. Control.* **2018**, *24*, 2970–2985. [CrossRef]
27. Timoshenko, S.P. *Vibration Problems in Engineering*; D. van Nostrand Company Inc.: New York, NY, USA, 1937.
28. Wu, J.L. *Elasticity Theory*; Higher Education Press: Beijing, China, 2022.
29. Banerjee, J.R.; Sobey, A.J. Dynamic stiffness formulation and free vibration analysis of a three-layered sandwich beam. *Int. J. Solids Struct.* **2005**, *42*, 2181–2197. [CrossRef]
30. Mead, D.M. Wave propagation in continuous periodic structures: Research contributions from Southampton, 1964–1995. *J. Sound Vib.* **1996**, *190*, 495–524. [CrossRef]
31. Wen, X.S. *Phononic Crystals*; National Defense Industry Press: Beijing, China, 2009.

Disclaimer/Publisher's Note: The statements, opinions and data contained in all publications are solely those of the individual author(s) and contributor(s) and not of MDPI and/or the editor(s). MDPI and/or the editor(s) disclaim responsibility for any injury to people or property resulting from any ideas, methods, instructions or products referred to in the content.